

In-situ Raman spectroscopy analysis of the interfaces between Ni-based SOFC anodes and stabilized zirconia electrolyte



D.A. Agarkov ^{*}, I.N. Burmistrov, F.M. Tsybrov, I.I. Tartakovskii, V.V. Kharton, S.I. Bredikhin

Institute of Solid State Physics RAS, 2 Academician Osipyan Str., Chernogolovka 142432, Moscow Distr., Russia

ARTICLE INFO

Article history:

Received 30 July 2016

Received in revised form 9 December 2016

Accepted 23 December 2016

Available online 10 January 2017

Keywords:

Raman spectroscopy

SOFC

Anode electrolyte interface

ABSTRACT

A novel experimental approach for *in-situ* Raman spectroscopy of the electrode | solid electrolyte interfaces in controlled atmospheres, based on use of the optically transparent single-crystal membranes of stabilized cubic zirconia, was proposed and validated. This technique makes it possible to directly access the electrochemical reaction zone in SOFCs by passing laser beam through the single-crystal electrolyte onto the interface, in combination with simultaneous electrochemical measurements. The case study centered on the analysis of NiO reduction in standard cermet anodes under open-circuit conditions, demonstrated an excellent agreement between the observed kinetic parameters and literature data on nickel oxide. The porous cermet reduction kinetics at 400–600 °C in flowing H₂-N₂ gas mixture can be described by the classical Avrami model, suggesting that the reaction rate is determined by metal nuclei growth limited by Ni diffusion. The advantages and limitations of the technique are briefly addressed.

© 2017 Elsevier B.V. All rights reserved.

1. Introduction

Redox kinetics and local variations in the charge carrier concentration gradients across the electrode | electrolyte interface are among key factors determining performance of solid oxide fuel cell (SOFC) electrodes [1–3]. Although microscopic mechanisms of the electrode reactions can be evaluated by numerous electrochemical methods, the resultant information is usually cumulative, except for the microelectrode techniques. One important complementary technique enabling real-time analysis of the SOFC reactions is the Raman spectroscopy, successfully applied for a variety of model systems, processes and fuel cell materials [4–13]. Due to low penetration depth of the excitation radiation, however, most approaches known in literature (e.g., [5–13]) are mainly based on the Raman spectra collected from the outer boundaries of model electrochemical cells, primarily surfaces of the electrodes and solid electrolyte membranes. The electrochemical reaction zones where ionic and electronic charge carriers are generated, such as the triple-phase boundary (TPB) area, may hardly be achieved to a sufficient extent by viewing the surfaces and edges of the electrode systems.

Following our previous reports on the developments and validation of a new combined technique for *in-situ* Raman spectroscopy of the electrode | solid electrolyte interfaces under SOFC operating conditions [14,15], the present work is centered on the studies of reduction kinetics of standard Ni-based cermet anodes applied onto optically transparent single-crystal membranes of 10 mol% Sc₂O₃ and 1% mol% Y₂O₃ stabilized

zirconia (10Sc1YSZ). An appropriate selection of the electrode geometry and solid electrolyte (SE) membrane makes it possible to directly collect Raman spectra from the TPB zone, by passing the beam through single crystal electrolyte onto the anode | electrolyte interface. The results, briefly summarized in the present work, correspond to the open-circuit conditions; their comparison with the behavior of polarized anode layers will be reported elsewhere.

2. Experimental

In order to explain operation principles of the experimental setup elaborated for *in-situ* Raman spectroscopy analysis of the interfaces as function of temperature, atmosphere and current density, Fig. 1 compares the planar SOFC electrode configuration (a) with that of the model electrochemical cells used in this work (b). The working electrode (WE) made of Ni-based cermet for these case studies, has a standard circular shape; the ring-shape counter electrode (CE) enables penetration of the laser beam through the transparent SE membrane. The planar electrochemical cells were hermetically sealed by KeraGlas ST K02 glass tape (Kerafol, Germany) onto a single-crystal sapphire tube, with two thermocouples and Pt current collectors (Fig. 1c). Fig. 1d shows a general scheme of the entire setup, which comprises a gas-mixing system equipped with mass-flow controllers (MFC, Bronkhorst), high-temperature chamber (Fig. 1c), and an optical system. Raman scattering in the WE zone was excited by a 30 mW green (532 nm) laser. The Raman spectra presented in this work were obtained as sum of 100 spectra collected for 0.5–2 s each, depending on temperature; the background spectra were automatically subtracted. The

^{*} Corresponding author.

E-mail address: agarkov@issp.ac.ru (D.A. Agarkov).

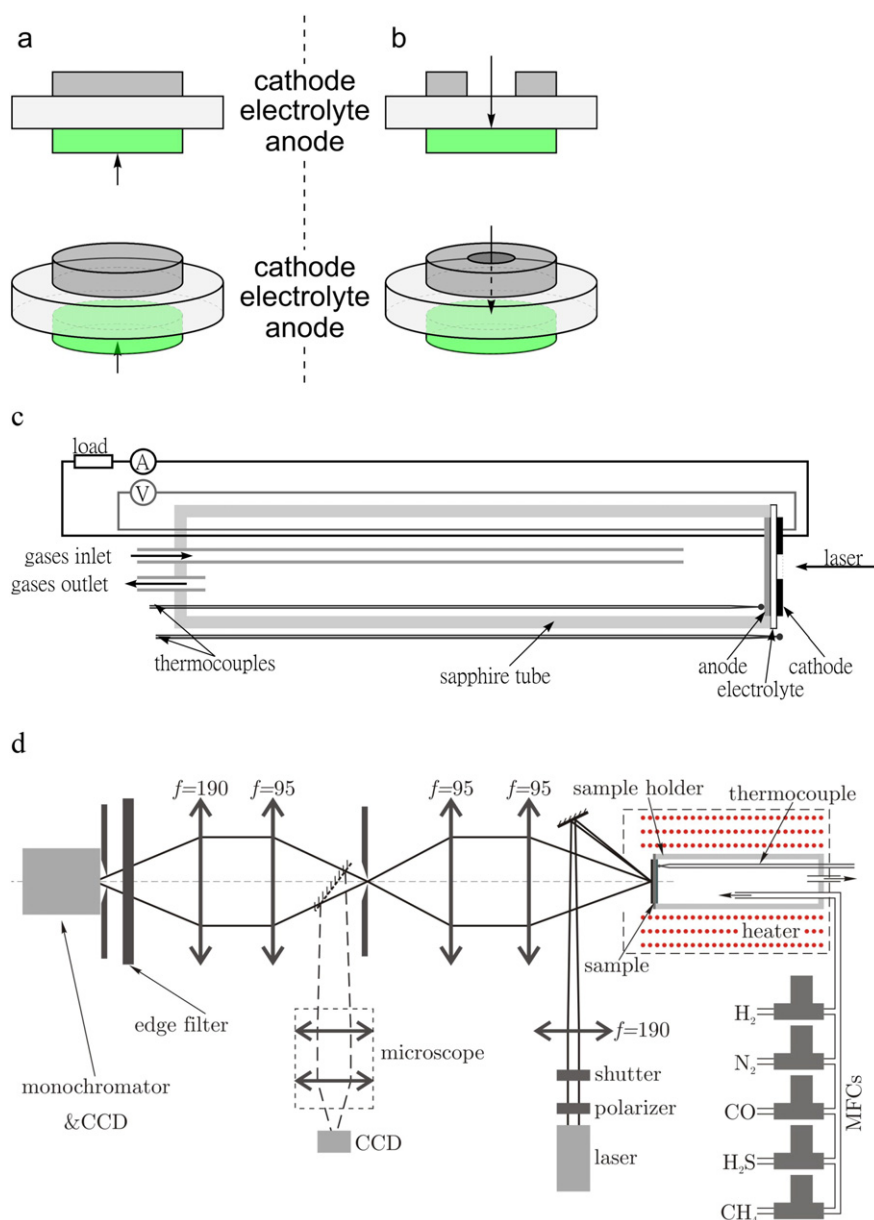


Fig. 1. Electrode configuration in standard planar fuel cells (a); and model cell for the studies of the solid electrolyte | anode interface based on optically transparent solid electrolyte membrane (b), and schematic drawings of the high-temperature holder of the model cells (c) and entire experimental setup for the Raman spectroscopy studies (d).

equipment and measurement procedures were described in previous publications [14,15].

The transparent SE membranes (thickness of 250 and 500 μm) were cut from 10Sc1YSZ single crystals, grown by the direct melt crystallization technique in a cold crucible at the Institute of General Physics RAS [16,17]. The cubic fluorite-type structure of the electrolyte crystals was confirmed by the Laue method; one pattern is presented in Fig. 2a. Optical transparency of the polished membranes was assessed measuring their transmittance spectra (Specord M40 spectrophotometer, Carl Zeiss Jena). In the wavelength range of 540–600 nm, the transmittance was about 70%, high enough to obtain Raman spectra from the WE | SE interface.

The composition, thickness, microstructure and deposition route of Ni-based cermet anodes were optimized in previous works [18,19]. Submicron NiO powder (Sigma Aldrich) was preliminary annealed in air at 700 $^{\circ}\text{C}$ for 2 h to remove overstoichiometric oxygen and absorbed water [20]. A mixture of pre-annealed NiO (40 wt%) and 10 mol% $\text{Sc}_2\text{O}_3 + 1 \text{ mol}\% \text{CeO}_2$ co-stabilized zirconia (10Sc1CeSZ, DKKK, Japan,

60 wt%) was ball-milled and then mixed with organic additives to prepare pastes for screen-printing. The porous anodes were deposited onto one side of the SE disks, dried at 130 $^{\circ}\text{C}$, and sintered in air at 1250 $^{\circ}\text{C}$ for 3 h. Reduction of the anodes was performed in the course of Raman measurements at working temperatures, namely 400, 450, 500, 550 and 600 $^{\circ}\text{C}$. CE was made of a submicron composite consisting of 60 wt% $(\text{La}_{0.8}\text{Sr}_{0.2})_{0.95}\text{MnO}_3$ (LSM) and 40 wt% 10Sc1CeSZ, as reported elsewhere [14,18]. Microstructure of the porous layers was characterized by scanning electron microscopy (SEM); X-ray diffraction (XRD) and energy dispersive spectroscopy (EDS) were employed to confirm that the phase and cation composition of the electrodes corresponds to nominal. XRD analysis showed an absence of phase impurities in the two-phase composites consisting of NiO and cubic zirconia solid solution. No cation impurities in the anode layers were identified in the EDS spectra within the detection limits of this technique. Description of the equipment and experimental procedures used for characterization can be found in Refs [14,18–20]. Typical anode microstructures are illustrated in Fig. 2b–d.

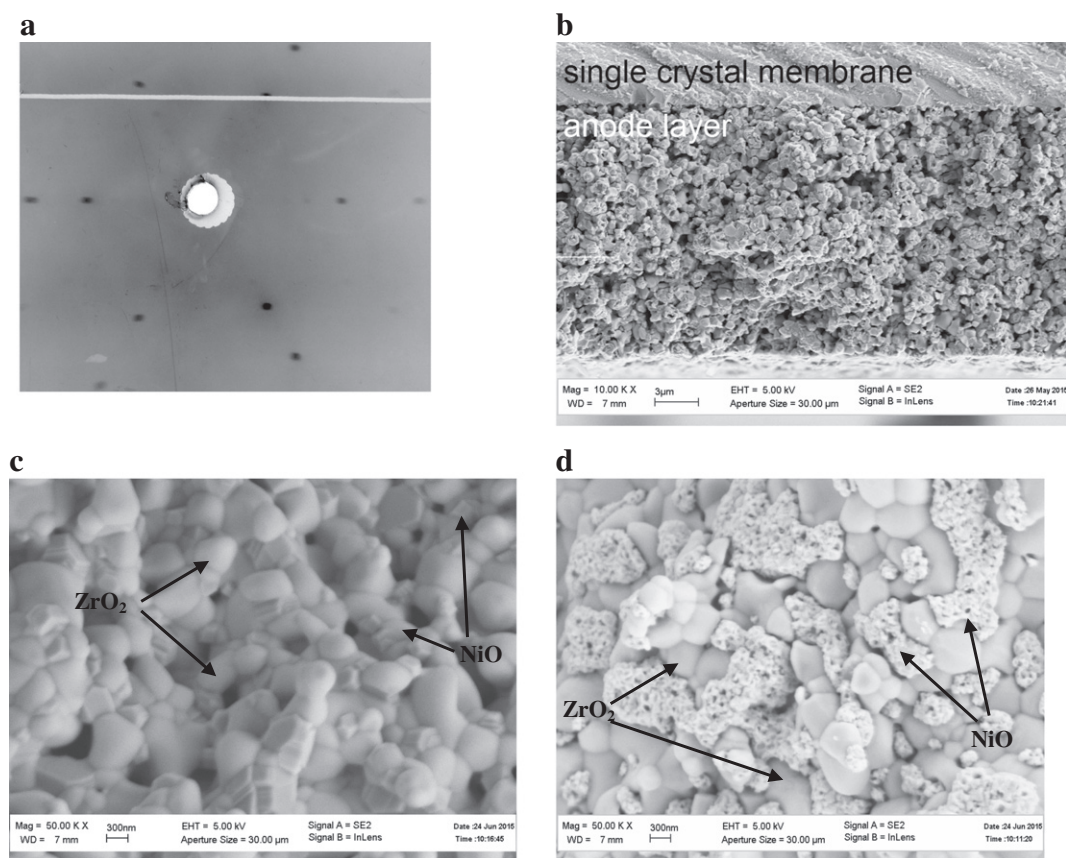


Fig. 2. Laue pattern of the 10Sc1YSZ single crystal membrane (a), SEM micrograph of fractured model electrochemical cell (b), and SEM images of as-prepared NiO-10Sc1CeSZ composite anode prior to reduction (c) and after redox cycling (d).

3. Results and discussion

Fig. 3a presents one representative example of the room-temperature Raman spectra collected from the interface between oxidized cermet anode and 10Sc1YSZ solid electrolyte membrane. The peak at approximately 515 cm^{-1} corresponds to 1P (1 phonon) oscillations in NiO [21]. The bands at ~ 740 , 860 and 1100 cm^{-1} are associated with 2P oscillations in nickel oxide, whilst the $\sim 1460\text{ cm}^{-1}$ peak originates from magnon (2M) oscillations. The strongest peak at $\sim 615\text{ cm}^{-1}$ corresponds to the sum of two contributions: NiO and cubic zirconia. Notice that similar overlapping of NiO and cubic ZrO_2 peaks is observed at $\sim 1100\text{ cm}^{-1}$. On the other hand, the 2M band totally disappears at the Neel temperature ($252\text{ }^\circ\text{C}$) due to the transformation of antiferromagnetic nickel oxide into the cubic β -NiO polymorph. At elevated temperatures when the noise level becomes high, intensity of the 515 , 740 and 860 cm^{-1} peaks is insufficient for quantitative analysis of the redox kinetics, based on determination of kinetic parameters (e.g., reduction time and rate) from the intensity vs. time dependencies after changing oxygen chemical potential over the electrode. Even for oxidized NiO, the intensity | background ratio of these peaks at 500 – $600\text{ }^\circ\text{C}$ becomes lower than 2, a rough criterion for the signal selection. Hence, the reduction degree of NiO at the interface can only be evaluated from the relative intensities of 615 and 1100 cm^{-1} peaks after subtraction of the cubic ZrO_2 contribution. The latter can be done by subtracting the final spectra, collected on total reduction of the cermet when all NiO is converted into metallic Ni. This transformation of the Raman spectra was made after each reduction cycle. Fig. 3b shows the variations of NiO subspectra with time during reduction in flowing $50\%\text{ H}_2$ – $50\%\text{ N}_2$ gas mixture at $500\text{ }^\circ\text{C}$.

Time dependences of the 615 cm^{-1} signal intensity on reduction of the cermet anode at 400 – $600\text{ }^\circ\text{C}$ are presented in Fig. 3c;

3d displays the intensity dependence on both temperature and time. In the course of Raman measurements, each reduction cycle was followed by re-oxidation in air at $900\text{ }^\circ\text{C}$, cooling down to a given temperature and continuous monitoring of the spectra in order to check reproducibility of the observed behavior. One should mention that reproducible kinetic parameters can only be obtained after initial redox cycling, which is accompanied with substantial morphological reconstruction of NiO (Fig. 2c, d). Prior to the first reduction, the as-prepared anode layer consists of sub-micron particles of cubic zirconia and nickel oxide; their size varies in the range 300 – 800 nm (Fig. 2c). Redox cycling leads to the formation of relatively large (up to several microns) and porous agglomerates of NiO, Fig. 2d. The sintered zirconia matrix remains essentially unchanged, as expected. Fig. 4 shows the Raman peak intensity vs. time dependencies for the first 3 redox cycles of an as-prepared electrode at $500\text{ }^\circ\text{C}$. Due to the microstructural reconstruction, primarily grain growth and agglomeration, the initial reduction rate is much slower compared to the 2nd and 3rd cycles when the reaction kinetics become stable. In addition to the stabilization of particle size, the increased reduction rate may be contributed by the relatively large porosity of nickel oxide agglomerates (Fig. 2d), although the role of the latter factor requires seems less critical.

As expected, the cermet reduction rate tends to exponentially increase on heating. The dependence of NiO reduction time (t_r) on reciprocal temperature is presented in Fig. 5a. The apparent activation energy, $1.7 \pm 0.2\text{ eV}$, is close to the activation energy of ^{63}Ni isotope diffusion along grain boundaries in NiO [22]. This behavior is consistent with literature data [23–26], which show that the kinetics of nickel oxide transformation into metallic Ni at intermediate temperatures is essentially determined by the cation transport and reaction rates at

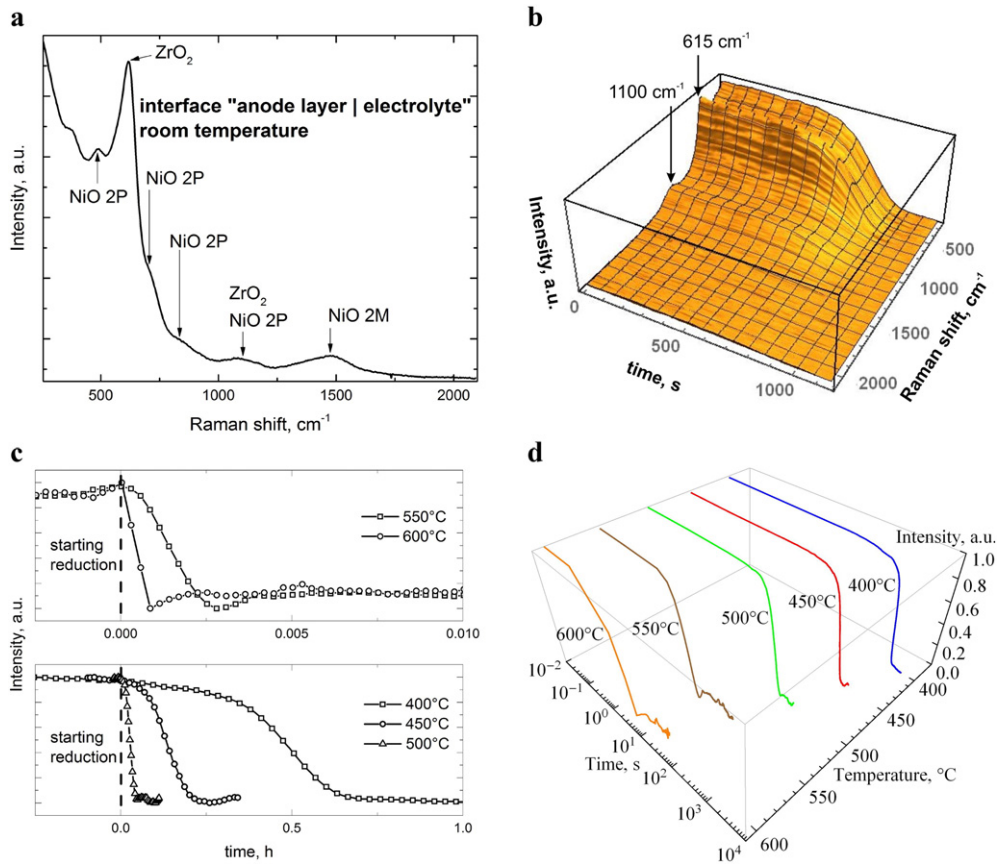


Fig. 3. Example of the room-temperature Raman spectra collected from as-sintered anode | electrolyte interface before reduction (a), Raman spectra taken from the interface as a function of time during reduction at 500 °C (b), and time dependences of 610 cm^{-1} peak intensity on reduction at 400–600 °C (c, d). For (b), the spectra are shown with subtracted final spectra (see text).

NiO | Ni boundaries. Such kinetics can be analyzed using the Avrami model [25,26]:

$$\ln(-\ln(1-\alpha)) = \ln k + n \ln t \quad (1)$$

where α is dimensionless reaction degree, k is the rate constant, and n is the exponent reflecting microscopic mechanisms of the entire process. One example of the Avrami plot is presented in Fig. 5b. This curve

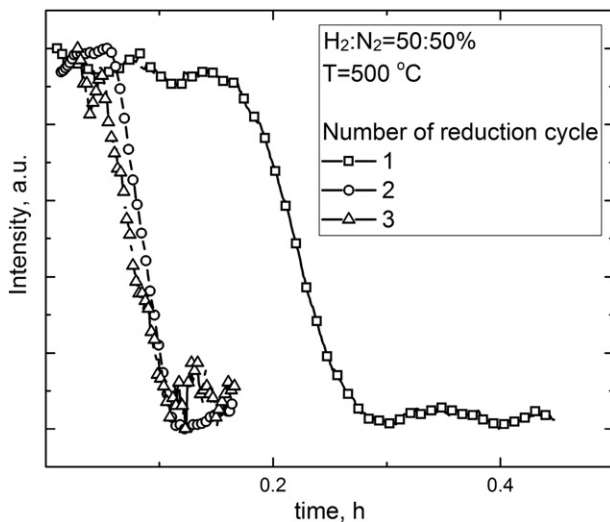


Fig. 4. Time dependences of the NiO peak intensity on anode reduction during the 1st, 2nd and 3rd redox cycles.

exhibits three distinct regions. The initial, non-linear part is related to the transient process when hydrogen diffuses into porous anode; the non-linear behavior at the final stage can be ascribed to decreasing penetration depth of the laser beam excitation due to covering of the grain surface by metallic Ni. The linear intermediate region of the Avrami plot corresponds to the n value of 1.33 ± 0.01 , again in excellent agreement with literature [23,26]. The relevant mechanism may be associated with the metal nuclei growth limited by Ni diffusion [25,26]. Therefore, under open-circuit conditions the kinetics of NiO reduction at the porous cermet anode | solid electrolyte interface is similar to that of the bulk reaction, as expected. These results are considered to validate the experimental approach proposed for the *in-situ* Raman spectroscopy studies.

4. Conclusions

The kinetics of NiO reduction at the cermet anode | ZrO_2 -based solid electrolyte interface under open-circuit conditions was assessed by the Raman spectroscopy at 400–600 °C. This work was centered on validation of a novel experimental approach for *in-situ* analysis of the inner interfaces in SOFCs under operating conditions, employing optically transparent single-crystal membranes of stabilized cubic zirconia. The case studies made it possible to obtain reliable data on NiO reduction, which agree with the kinetic parameters and microscopic mechanisms known in literature. After initial microstructural reconstruction on redox cycling, the behavior of standard cermet anodes in flowing H_2 - N_2 atmosphere can be described by the classical Avrami model. The new setup and the obtained kinetic data will be used to analyze relationships between the overpotential, anode oxidation degree and

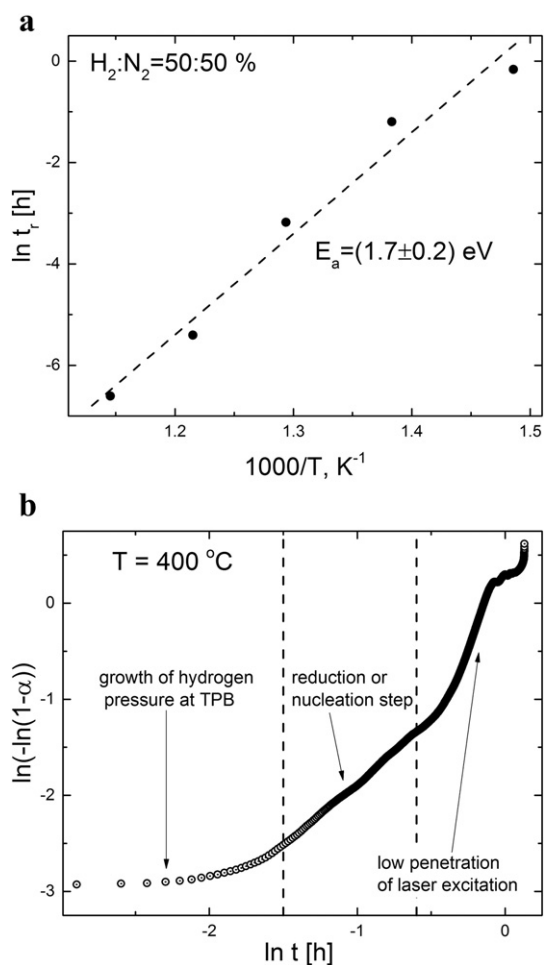


Fig. 5. Temperature dependence of the total reduction time of NiO-10Sc1CeSZ composite anode (a) and characteristic shape of the Raman intensity vs. time dependence plotted in Avrami coordinates (b).

SOFC operation regimes, which will be reported in a series of forthcoming publications.

Acknowledgements

This work was supported by the Ministry of Education and Science of the Russian Federation (Studies and Developments on Priorities of

Science and Technology federal program, unique identifier of the agreement RFMEFI61014X0007).

References

- [1] N.Q. Minh, T. Takahashi, Science and Technology of Ceramic Fuel Cells, Elsevier, Amsterdam, 1995.
- [2] J.A. Kilner, S.J. Skinner, S.J.C. Irvine, P.P. Edwards (Eds.), Functional Materials for Sustainable Energy Applications, Woodhead Publ., Oxford, 2012.
- [3] V.V. Kharton (Ed.), Solid State Electrochemistry II: Electrodes Interfaces and Ceramic Membranes, Wiley-VCH, Weinheim, 2011.
- [4] J. Yarwood, R. Douthwaite, S. Duckett (Eds.), Spectroscopic Properties of Inorganic and Organometallic Compounds: Techniques, Materials and Applications, Vol. 43, RSC, Cambridge, 2012.
- [5] M.B. Pomfret, J.C. Owrutsky, R.A. Walker, Anal. Chem. 79 (2007) 2367.
- [6] Z. Cheng, M.L. Liu, Solid State Ionics 178 (2007) 925.
- [7] M.B. Pomfret, J. Marda, G.S. Jackson, B.W. Eichhorn, A.M. Dean, R.A. Walker, J. Phys. Chem. C 112 (2008) 5232.
- [8] B.C. Eigenbrodt, M.B. Pomfret, D.A. Steinhurst, J.C. Owrutsky, R.A. Walker, J. Phys. Chem. C 115 (2011) 2896.
- [9] J.D. Kirtley, D.M. Halat, M.D. McIntyre, B.C. Eigenbrodt, R.A. Walker, Anal. Chem. 84 (2012) 9745.
- [10] Y. Kim, J.H. Kim, J. Bae, C.W. Yoon, S.W. Nam, J. Phys. Chem. C 116 (2012) 13281.
- [11] H. Kishimoto, K. Yashiro, T. Shimonosono, M.E. Brito, K. Yamaji, T. Horito, H. Yokokawa, J. Mizusaki, Electrochim. Acta 82 (2012) 263.
- [12] G. Schiller, C. Auer, W.G. Bessler, C. Christenn, Z. Ilhan, P. Szabo, H. Ax, B. Kapadia, W. Meier, J. Appl. Phys. B 111 (2013) 29.
- [13] M. Nagai, F. Iguchi, S. Onodera, N. Sata, T. Kawada, H. Yugami, ECS Trans. 35 (2011) 519.
- [14] D.A. Agarkov, I.N. Burmistrov, F.M. Tsybrov, I.I. Tartakovskii, V.V. Kharton, S.I. Bredikhin, V.V. Kveder, ECS Trans. 68 (2015) 2093.
- [15] D.A. Agarkov, I.N. Burmistrov, F.M. Tsybrov, I.I. Tartakovskii, V.V. Kharton, S.I. Bredikhin, Russ. J. Electrochem. 52 (2016) 600.
- [16] M.A. Borik, E.E. Lomonova, V.V. Osiko, V.A. Panov, O.E. Porodnikov, M.A. Vishnyakova, Y.K. Voron'ko, V.V. Voronov, J. Cryst. Growth 275 (2005), e2173.
- [17] V.I. Aleksandrov, V.V. Osiko, A.M. Prokhorov, V.M. Tatarintsev, Russ. Chem. Rev. 47 (1978) 213.
- [18] I. Burmistrov, D. Agarkov, S. Bredikhin, Y. Nepochatov, O. Tiunova, O. Zadorozhnaya, ECS Trans. 57 (2013) 917.
- [19] D.A. Agarkov, M.Sc. Thesis, Moscow Institute of Physics and Technology, Chernogolovka, Russia, 2013.
- [20] I. Burmistrov, D. Agarkov, I. Tartakovskii, V. Kharton, S. Bredikhin, ECS Trans. 68 (2015) 1265.
- [21] N. Mironova-Ulmane, A. Kuzmin, I. Steins, J. Grabis, I. Sildos, M. Pars, J. Phys. Conf. Ser. 93 (2007) 012039.
- [22] A. Atkinson, R.I. Taylor, Philos. Mag. A 43 (1981) 979.
- [23] A.F. Benton, P.H. Emmett, J. Am. Chem. Soc. 46 (1924) 2728.
- [24] J. Bandrowski, C.R. Bickling, K.H. Yang, O.A. Hougen, Chem. Eng. Sci. 17 (1962) 379.
- [25] S.F. Hulbert, J. Brit. Ceram. Soc. 6 (1969) 11.
- [26] J.T. Richardson, R. Scates, M.V. Twigg, Appl. Catal. A.Gen. 246 (2003) 137.